DFT-based analysis of the structural, electronic, optical, mechanical and thermodynamic characteristics of Rb_2YAuX_6 (X = Br, Cl) double perovskites for energy conversion applications

A. Merrad[a], H. Bouchenafa[a] and B. Benichou[b,c,*]

[a]*Laboratory for Theoretical Physics and Material Physics, Department of Physics, Faculty of Exact Sciences and Informatics, Hassiba Benbouali University of Chlef, Chlef 02000, Algeria.*

[b]*Department of Electronics, Faculty of Technology, Hassiba Benbouali University of Chlef, Chlef 02000, Algeria.*

[c]*Computational Materials Physics Laboratory, Faculty of Exact Sciences, Djillali Liabès University of Sidi Bel Abbès, Sidi Bel Abbès 22000, Algeria.*

[*]*e-mail: boucif_benichou@yahoo.fr*

Received 24 June 2025; accepted 25 August 2025

We investigated the potential of double perovskite halides Rb_2YAuX_6 (X = Br, Cl) for renewable energy applications using density functional theory (DFT) with the full-potential linearized augmented plane wave (FP-LAPW) method. These compounds are structurally stable in the cubic Fm-3m phase and demonstrate excellent mechanical strength. Electronic structure calculations revealed that the compounds are indirect band gap semiconductors, with energy gaps ranging from 1.58 to 2.01 eV when using the PBE-GGA approximation, and from 3.49 to 3.70 eV when using the TB-mBJ potential. Optical analysis shows strong ultraviolet (UV) absorption and low reflectivity in the visible range. We estimated the thermodynamic properties as a function of temperature using the quasi-harmonic Debye model. Key thermal parameters, including entropy, specific heat capacity, and Debye temperature, were calculated to evaluate thermal stability at high temperatures. These results are crucial to evaluate the suitability of Rb_2YAuX_6 compounds (X = Br, Cl) for use in industrial and high-temperature environments. This work represents the first predictive theoretical investigation of these materials, as no prior experimental or computational studies have been conducted on them. Our findings suggest that these double perovskites could be ideal for next-generation photovoltaic and energy harvesting applications.

Keywords: Double perovskites; ab initio calculations; FP-LAPW; TB-mBJ; optical; thermodynamic.

DOI: https://doi.org/10.31349/RevMexFis.72.040501

1. Introduction

In light of the global shift towards sustainable energy and the urgent need to minimize environmental damage, research on energy-efficient materials to replace fossil fuels has intensified [1]. One of the most promising candidates is perovskite-based materials which have exceptional potential for use in applications such as photovoltaics, light-emitting diodes, radiation detectors, and thermoelectric devices. Perovskite solar cells (PSCs) in particular have attracted substantial attention because of their high power conversion efficiencies of over 25%, low-cost fabrication methods, and versatility in material design [2]. However, the practical deployment of organic-inorganic hybrid perovskites such as $CH_3NH_3PbI_3$ is hindered by several challenges. These include poor chemical stability when exposed to heat and humidity, and the toxicity of lead ions [3,4].

To address these limitations, double perovskites have emerged as a promising alternative. They offer improved environmental stability, reduced toxicity and greater compositional flexibility. Defined by the general formula $A_2BB'X_6$, these materials enable toxic lead to be substituted with less harmful elements [5,6], allowing the production of thermally stable, lead-free compounds [7]. In addition to their optoelectronic capabilities, double perovskites exhibit favorable thermodynamic properties, including high thermal stability and beneficial heat capacity characteristics - both of which are essential for efficient, durable energy conversion systems. Thanks to their tunable optoelectronic and thermodynamic properties, double perovskites are attracting increasing interest for use in photovoltaic, fuel cells, sensors, catalysis and thermoelectric devices [8,9].

Recent advancements in halide-based double perovskites have significantly expanded the range of materials available for clean energy applications. Typically represented by the formula $A_2M(I)M(III)X_6$ [10], these materials are emerging as a viable alternative to lead-based perovskites due to their enhanced stability, adjustable electronic properties, and lower toxicity. For instance, Rodrigues *et al*. [11] synthesized and characterized the lead-free double perovskite $Cs_2AgSbCl_6$, revealing it to have a stable cubic structure and an indirect band gap of around 2.7 eV, as well as good thermal stability. This highlights its potential for use in optoelectronic applications. Similarly, Volonakis *et al*. [12] investigated $Cs_2BB'X_6$ compounds (B = Bi, Sb; B' = Cu, Ag, Au; X = Cl, Br, I) and found that they have low effective carrier masses and tunable visible-range band gaps, rendering them suitable for light-harvesting technologies.

Feng *et al*. [13] also reported on the cubic phase of Cs_2CuBiX_6 (X = Cl, Br), which exhibited indirect band gaps and reasonable stability under thermal stress, illumination, and humidity. McClure *et al*. [14] reported band gaps of 2.19 and 2.77 eV for $Cs_2AgBiBr_6$ and $Cs_2AgBiCl_6$, respectively. These values are slightly lower than those of $CH_3NH_3PbBr_3$ (2.26 eV) and $CH_3NH_3PbCl_3$ (3.00 eV). Subsequently, Wang *et al*. [15] demonstrated that $Cs_2AgBiBr_6$-based perovskite solar cells (PSCs) achieved a power conversion efficiency of 3.11%, which is one of the highest for thermally stable, lead-free devices.

While this efficiency is moderate, it has prompted the exploration of alternative structures, such as Cs_2AgSbX_6 and Y_2AgXZ_6 (Y = K, Rb, Na, Li; X = Sb, Bi and Z = halogen) [16,17]. While cation substitution (*e.g*., $Bi^{3+} \rightarrow Sb^{3+}$ or $Cs^+ \rightarrow$ lighter alkali metals) can improve optoelectronic behavior, the indirect band gaps of these devices restrict their photovoltaic performance. However, incorporating indium has shown potential for inducing an indirect-to-direct band gap transition, thereby improving light absorption and device efficiency [18]. Alongside experimental studies, computational approaches such as density functional theory (DFT) have become critical tools for predicting the structural, electronic, and thermoelectric behavior of new perovskite systems. Saeed *et al*. [19] conducted an extensive DFT analysis on Cs_2AgCrX_6 (X = Cl, Br, I), revealing promising structural, electrical, mechanical, optical, and thermoelectric properties for potential energy applications. Further theoretical investigations have focused on understanding the electronic, optical, and transport properties of other halide double perovskites, including Rb_2XInBr_6 (X = Na, K) [20], $Rb_2ScCuBr_6$ and $Cs_2ScCuBr_6$ [21], and K_2AgSbX_6 (X = Cl, Br) [22]. These investigations have enriched the compositional landscape of double perovskites and laid a solid theoretical foundation for future experimental efforts and material optimization. This study primarily aims to use DFT-based computational methods to predict new, lead-free double perovskite materials that exhibit enhanced optoelectronic and charge transport properties for use in energy applications. This work focuses on the structural stability, thermodynamic behavior, elastic response, and electro-optic characteristics of Rb2YAuX6 (X = Br, Cl) compounds. Particular attention is given to evaluating the impact of halide substitution on these critical physical parameters. To our knowledge, no prior theoretical or experimental investigations have been conducted on these specific materials. This study is expected to provide valuable information for designing and developing environmentally friendly double perovskites for use in future thermoelectric systems and solar energy technologies.

2. Calculation method

This study investigated the structural, mechanical, electronic, optical, and thermodynamic properties of the double perovskites Rb_2YAuX_6 (X= Br,Cl) using the WIEN2k computational package. This package is based on density functional theory (DFT) within the full-potential linearized augmented plane wave (FP-LAPW) formalism [23]. This method solves the Kohn–Sham equations, derived from the Schrödinger wave equation, and treats the electronic wave function as a functional of the electron density. Within the muffin-tin spheres centered on atoms, the wave functions are expanded using spherical harmonics, while in the interstitial regions they are represented by plane-wave expansions, assuming a constant potential in each region. For structural optimization and ground-state energy calculations, the Perdew–Burke–Ernzerhof generalized gradient approximation (PBE-GGA) [24] and the PBE functional revised for solids (GGA-PBEsol) [25] were used, despite their well-known tendency to underestimate electronic band gaps. We selected the PBE-GGA functional as our primary method because it is robust and widely adopted in computational solid-state physics. It provides a reliable and computationally efficient framework for analyzing a broad range of properties, including structural and mechanical characteristics. We are aware that PBEsol is specifically optimized for solids and often yields more accurate lattice constants and bulk moduli. To enhance the reliability of our study, we performed additional structural optimization calculations using PBEsol. The results are presented in Table I.

TABLE I. The optimized lattice parameter a, bulk modulus B_0, its pressure derivative B_0', minimum energy E_0, and formation energy $E_{\rm form}$ for Rb_2YAuX_6 (X = Br, Cl) using PBE-GGA and PBEsol.

Compound	Phase	Method	a (Å)	B_0 (GPa)	B_0'	E_0 (Ry)	$E_{\rm form}$ (Ry)
Rb_2YAuBr_6	FM	PBE-GGA	11.3081	25.0801	2.4818	-88073.875177	-1.739
	FM	PBEsol	11.0709	31.1025	3.5768	-88031.397527	
	NM	PBE-GGA	11.3083	24.9879	2.1704	-88073.875186	
	NM	PBEsol	11.0689	29.5174	4.9199	-88031.398618	
Rb_2YAuCl_6	FM	PBE-GGA	10.7634	30.1263	4.7595	-62332.365791	-2.033
	FM	PBEsol	10.5504	34.3315	5.1422	-62302.247853	
	NM	PBE-GGA	10.7633	30.2241	4.9683	-62332.365800	
	NM	PBEsol	10.5544	34.4985	4.1812	-62302.248317	

However, standard GGA functionals are known to underestimate band gaps. To overcome this issue, we complemented our calculations with the Tran–Blaha modified Becke–Johnson (TB-mBJ) potential [26], which significantly improves electronic band-structure predictions. This dual-functional strategy allowed us to use PBE-GGA (and PBEsol for validation) for structural and mechanical properties, while employing mBJ for a more accurate description of the electronic and optical properties. The Monkhorst–Pack scheme was used to sample the first Brillouin zone [27]. A $10 \times 10 \times 10$ k-point mesh was used for electronic structure calculations, and a $20 \times 20 \times 20$ mesh for evaluating optical properties. The parameters $G_{\max}$ and $\mathrm{R_{MT}} \times \mathrm{K_{max}}$ were set to 14 and 8, respectively. Here, $\mathrm{R_{MT}}$ represents the radius of the smallest atomic sphere. These parameters are crucial for defining the basis-set cutoff and ensuring the precision of the LAPW method. The energy convergence threshold was set to 10^{-4} Ry, with total charge convergence maintained at 10^{-4} e.

The elastic constants were calculated using the cubic-elastic package implemented in WIEN2k [28], which computes the three independent elastic constants C_{11}, C_{12}, and C_{44} that characterize the mechanical response of cubic crystals under strain. Optical properties were obtained using the Kramers–Kronig relations, which connect the real and imaginary parts of the dielectric function [29].

The electronic configurations used in the simulations were:

$$\mathrm{Rb} : 4s^2\, 4p^6\, 5s^1,$$

$$\mathrm{Y} : 4s^2\, 4p^6\, 4d^1\, 5s^2,$$

$$\mathrm{Au} : 5d^{10}\, 6s^1,$$

$$\mathrm{Br} : 4s^2\, 4p^5,$$

This ensured accurate valence-electron interaction modeling. Finally, thermodynamic properties—entropy, specific heat capacity, and thermal expansion coefficient—were calculated using the Gibbs2 code [30], offering reliable predictions across wide temperature and pressure ranges.

3. Results and discussion

3.1. Structural stability

The structural feasibility of a double perovskite with the general formula $\mathrm{A_2BB'X_6}$ can be evaluated using two geometric descriptors: the tolerance factor (τ) and the octahedral factor (μ). These dimensionless parameters provide insight into the spatial compatibility of the constituent ions of the perovskite lattice and are defined as follows:

$$\tau = \frac{R_A + R_X}{\frac{\sqrt{2\,(R_B + R_{B'})} + R_X}{2}}, \tag{1}$$

$$\mu = \frac{R_B}{R_X}, \tag{2}$$

where R_A, R_B, and $R_{B'}$ are the ionic radii of the A-site monovalent cation, the trivalent B-site cation, and the B'-site cation, respectively, and R_X is the radius of the halide anion. These definitions were first proposed by Goldschmidt [31], and the ionic radii values used here follow the revised data by Shannon [32].

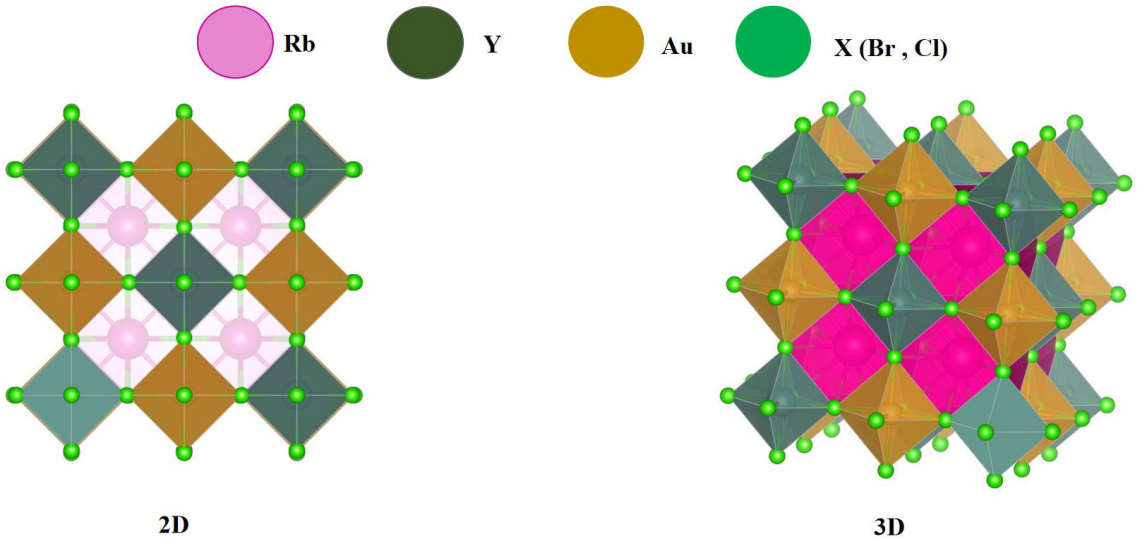

FIGURE 1. The atomic arrangement of the double perovskite $\mathrm{Rb_2YAuX_6}$ (X = Br, Cl) is shown in both 2D and 3D views.

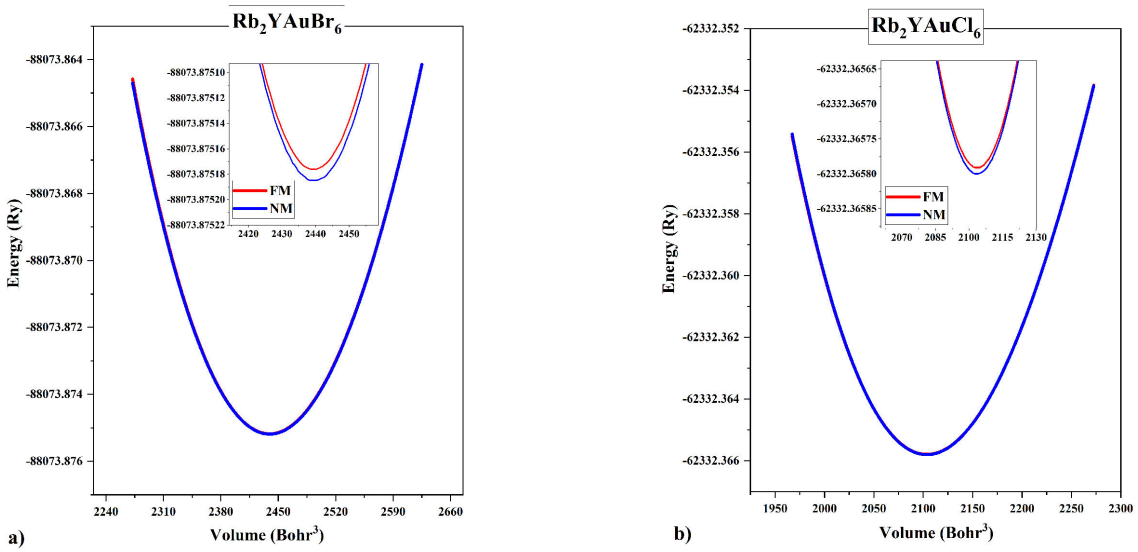

FIGURE 2. Calculated total energy as a function of the volume for a) Rb_2YAuBr_6 and b) Rb_2YAuCl_6 compounds in nonmagnetic (NM) and ferromagnetic (FM) configurations using the PBE-GGA approximation.

A tolerance factor in the range of 0.71 to 1.00 generally indicates the formation of a stable perovskite structure, with values close to 1.00 suggesting an ideal cubic geometry. Li *et al*. [33] calculated the tolerance factors for the Rb_2YAuX_6 (X = Br, Cl) compounds by taking into account the ionic radii of Rb^+ (1.52 Å), Y^{3+} (0.90 Å), Au^{3+} (0.85 Å), Br^- (1.96 Å) and Cl^- (1.81 Å). The resulting tolerance factors were found to be approximately 0.868 for X = Br and 0.878 for X = Cl. These values confirm the likelihood of forming a stable cubic perovskite structure in the $Fm\bar{3}m$ space group (No. 225) [34]. Figure 1 illustrates the atomic arrangement of the double perovskite Rb_2YAuX_6 (X = Br, Cl) is shown in 2D and 3D views. The crystallographic coordinates are as follows: Rb atoms occupy the position (1/4, 1/4, 3/4); Y atoms occupy the position (1/2, 0, 0); Au atoms occupy the position (0, 0, 0); and halide ions (Br, Cl) occupy the position (1/4, 0, 0). This configuration is consistent with a highly symmetric cubic perovskite phase.

The equation of state used to fit the calculated energy-volume data is given by the third-order Birch-Murnaghan equation:

$$E(V) = E_0 + \frac{B_0'}{B_0'(B_0'-1)} \times \left[V\left(\frac{V_0}{V}\right)^{B_0'} - V_0\right] + \frac{B_0}{B_0'}(V - V_0), \quad (3)$$

The equation incorporates several key parameters. V_0 represents the equilibrium volume (ground-state) of the unit cell, and V corresponds to the deformed volume. E_0 denotes the total energy in the ground state; B_0 is the bulk modulus; and B_0' is its first pressure derivative. Fitting the calculated energy-volume data using this formalism shows that the minimum point on the E-V curve corresponds to the configuration with the lowest energy, which represents the crystal's ground state. Figure 2 shows how the total energy varies with volume for the investigated compounds. To determine the most stable magnetic configuration, two spin states were examined: non-magnetic (NM) and ferromagnetic (FM). The results indicate that the paramagnetic configuration yields the lowest total energy, confirming that the paramagnetic phase obtained with the GGA functional corresponds to the optimized ground-state structure of the studied system.

Additionally, to investigate the relative phase stabilities for the physical properties of interest, we have calculated the ground-state stability by computing the formation energy of Rb_2YAuX_6 (X = Br, Cl) double perovskites [35]. to determine the formation energy and demonstrate the compounds' thermodynamic stability, we employ the following expression:

$$E_{\text{form}}^{\text{Rb}_2\text{YAuX}_6} = \frac{1}{10}\left(E_{\text{solid}}^{\text{Rb}_2\text{YAuX}_6} - [2E_{\text{Rb}} + E_{\text{Y}} + E_{\text{Au}} + 6E_{\text{X}}]\right), \quad (4)$$

The stability of the compound is confirmed by negative formation energies. From the computed negative formation energy values displayed in Table I, it can be inferred that the double perovskites Rb_2YAuX_6 (X = Br, Cl) are anticipated to exhibit thermodynamic stability and can therefore be synthesized experimentally.

3.2. Electronic properties

This section presents the electronic band structures of the halide double perovskites Rb_2YAuBr_6 and Rb_2YAuCl_6 (see Fig. 3). As illustrated in the band diagrams, the valence band maximum (VBM) and the conduction band minimum (CBM) do not occur at the same *k*-point. Both compounds exhibit an indirect bandgap: between the L and Γ points when using the

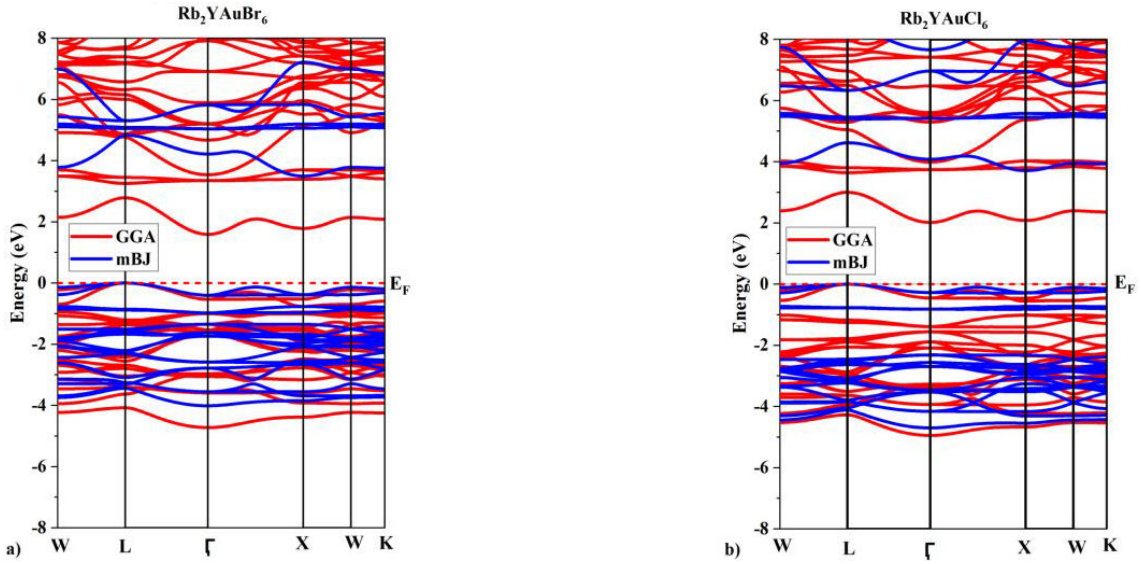

FIGURE 3. Electronic band structure plots for Rb_2YAuBr_6 [panel a)], and Rb_2YAuCl_6 [panel b)] obtained using both the GGA-PBE (red lines) and mBJ-GGA (blue lines) functionals.

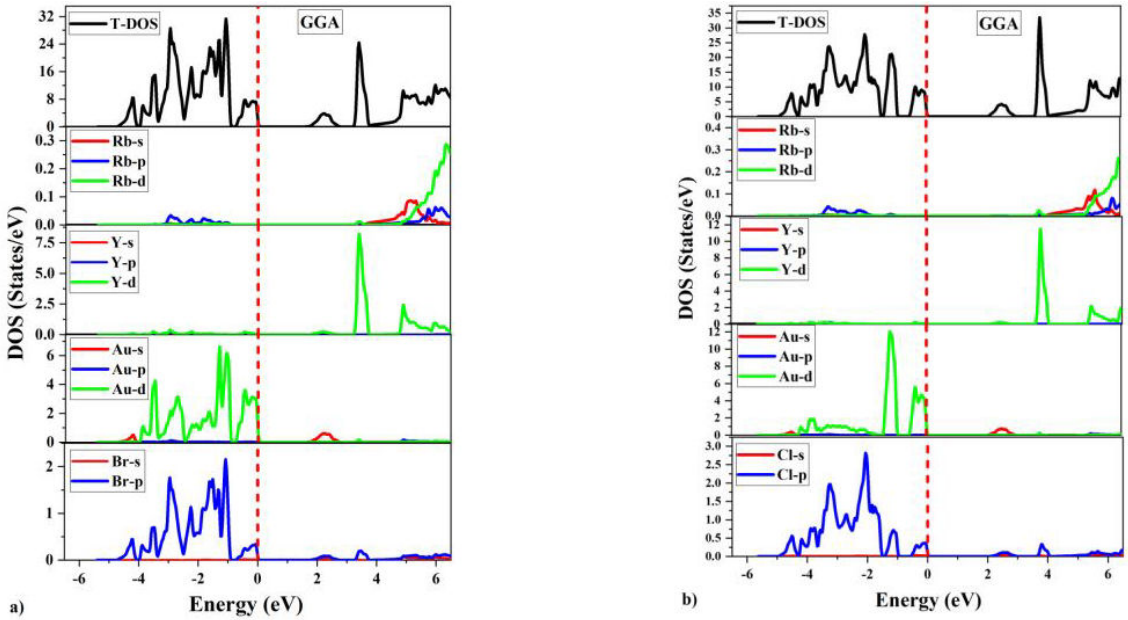

FIGURE 4. Total and partial density of states for (a) Rb_2YAuBr_6 and (b) Rb_2YAuCl_6 perovskites calculated by GGA.

GGA approach, and between the L and X points when applying the Tran–Blaha modified Becke–Johnson (TB-mBJ) potential. The mBJ approximation is a semi-local exchange potential specifically designed to improve the accuracy of bandgap predictions in semiconductors and insulators [26], where GGA typically underestimates these values. In many cases, the mBJ method yields bandgap energies that closely match experimental observations. Our results therefore confirm the indirect bandgap nature of the Rb_2YAuX_6 (X = Br, Cl) systems.

A significant discrepancy is observed between the bandgap values obtained using GGA (1.58–2.01 eV) and mBJ (3.49–3.70 eV). This difference arises from the distinct treatment of exchange-correlation effects: while GGA is computationally efficient, it systematically underestimates band gaps due to its limited description of electronic exchange interactions. in contrast, the mBJ potential introduces a non-local exchange term, providing a more realistic approximation of quasiparticle effects and resulting in bandgap values that are closer to the experimental results.furthermore, the trend of larger band gaps in Cl-based perovskites compared to Br-based ones is consistent with the higher electronegativity and smaller lattice constants of chloride compounds,which enhance electronic confinement.which enhance electronic confinement. Although mBJ does not fully replace advanced many-body techniques, it provides an excellent compromise

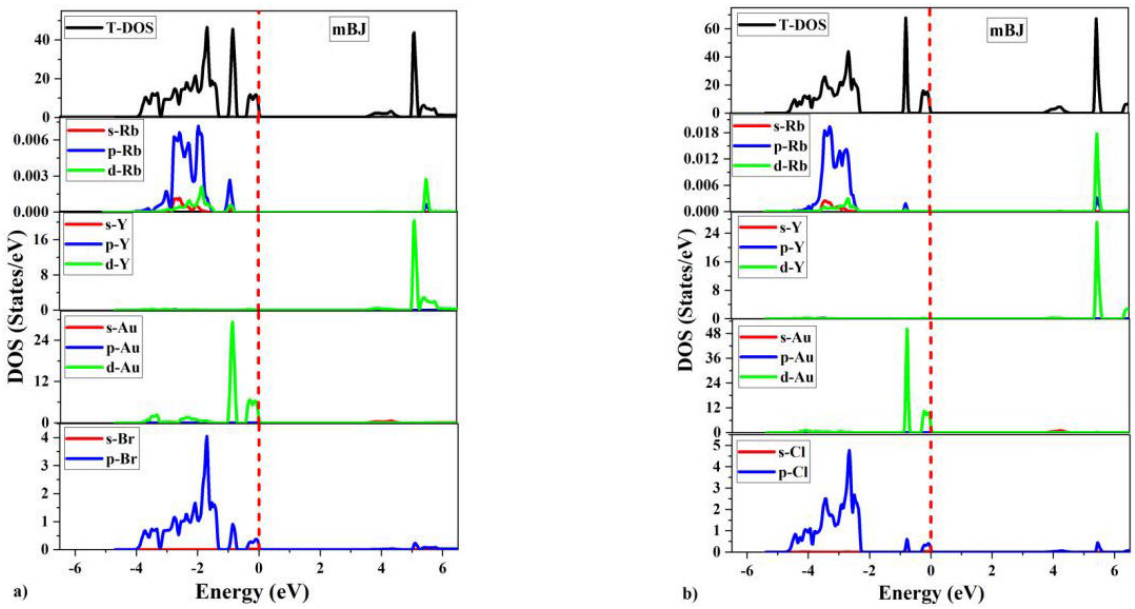

FIGURE 5. Total and partial density of states for a) Rb_2YAuBr_6 and b) Rb_2YAuCl_6 perovskites calculated by mBJ-GGA.

between accuracy and computational cost, making it a powerful tool for predicting the electronic properties of complex double-perovskite materials [36].

The comprehensive density of states (DOS) profiles, presented in Figs. 4 and 5, offer valuable insights into the electronic structure and orbital interactions of the Rb2YAuX6 (X = Br, Cl) double perovskites. Analysis shows that the valence band is predominantly influenced by the p-orbitals of the halogen atoms (Br or Cl) and the d-orbitals of the gold atoms (Au). Minor contributions are observed from the yttrium atom (Y), while the rubidium atom (Rb) exerts negligible influence. Near the Fermi level, the electronic states are predominantly attributed to the Au d-orbitals, accompanied by hybridization with the halogen p-orbitals. Meanwhile, the Rb and Y orbitals remain largely inactive in terms of direct electronic contribution. The lower conduction band is predominantly shaped by the hybridization of the halogen p-states and gold d-states, and to a lesser extent the yttrium s-states. This indicates covalent bonding in these materials. In Cl-based compounds, the valence band is narrower than in Br-based analogues due to the higher electronegativity of Cl. This reduces orbital overlap and increases the ionic character of the bonding. The alkali metal (Rb) primarily plays a structural role, ensuring lattice stability through ionic interactions, and its electronic states lie far from the Fermi level. Consequently, substitution with Cl does not significantly affect the band gap, though it may cause slight variations in lattice parameters due to differences in ionic radii. Comparative analysis of the GGA and mBJ approaches reveals that the mBJ functional predicts a notably wider band gap, particularly in Cl-based compounds. This enhancement is attributed to the mBJ functional's more accurate treatment of exchange-correlation effects. Furthermore, the mBJ functional increases the intensity of the density of states (DOS) associated with Au d-states near the Fermi level while reducing the DOS contribution of Cl p-states in the valence region [37].

3.3. Optical properties

To understand the optical behavior of the double perovskite compounds Rb_2YAuBr_6 and Rb_2YAuCl_6, we examined their frequency-dependent complex dielectric functions [38]. These functions are defined as

$$\epsilon(\omega) = \epsilon_1(\omega) + i\epsilon_2(\omega), \tag{5}$$

where $\epsilon_1(\omega)$ is the real part and $\epsilon_2(\omega)$ is the imaginary part [39]. We calculated these functions using the generalized gradient approximation (GGA) and the modified Becke-Johnson (mBJ) potential. Figures 6a) and 6b) show that the static dielectric constants ($\epsilon_1(0)$) are approximately 3.9 and 3.1 for Rb_2YAuBr_6 and Rb_2YAuCl_6, respectively. These values indicate moderate dielectric screening. They are also consistent with the calculated refractive indices, following the relation

$$n^2(0) \approx \epsilon_1(0), \tag{6}$$

[40]. The mBJ results show a reduction in $\epsilon_1(\omega)$ due to the larger predicted band gap. Figure 6b) shows that the imaginary part (ϵ_2) indicates strong interband transitions with absorption thresholds of approximately 3.7 and 4.2 eV under GGA. Under mBJ, these thresholds shift to approximately 4.8 and 5.3 eV, respectively. Most absorption occurs between 7.0 and 8.5 eV for Rb_2YAuBr_6 and between 6.0 and 7.5 eV for Rb_2YAuCl_6. The refractive index ($n(\omega)$) exceeds 1.8 at low energy and decreases with photon energy, consistent with normal dispersion. At the same time, the extinction coefficient $K(\omega)$ shows the attenuation of light through the investigated materials, as shown in Fig. 6a), 6b). The calculated values show that the overall patterns of both $K(\omega)$ and $\epsilon_2(\omega)$

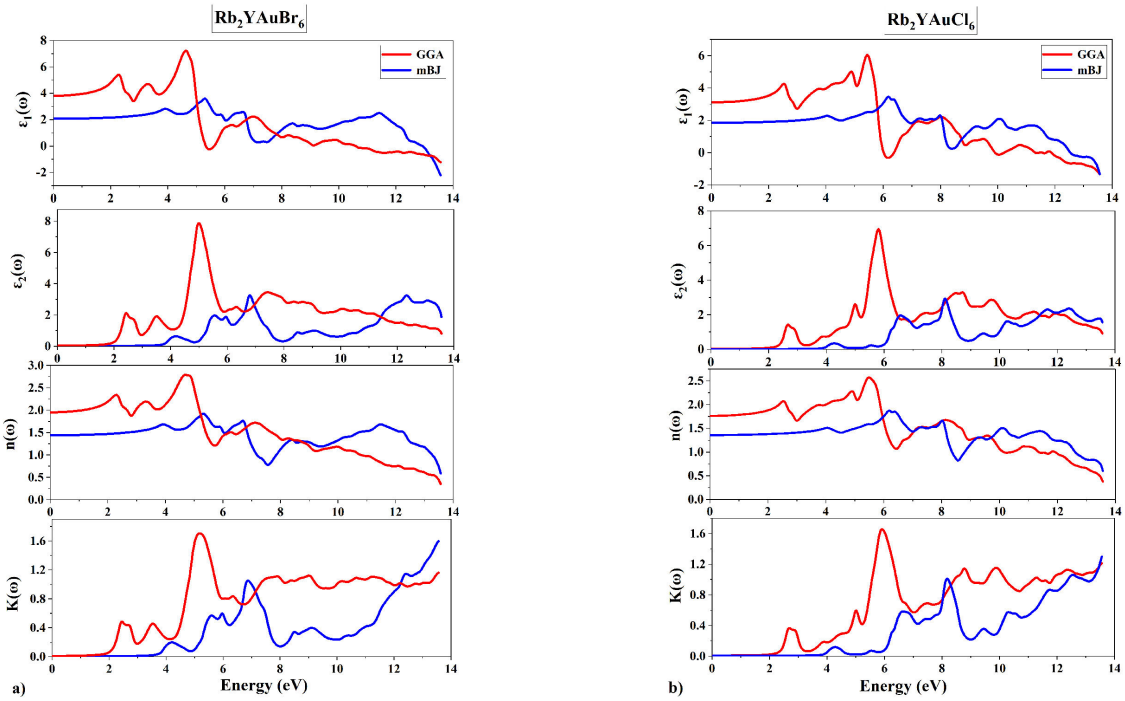

FIGURE 6. The calculated optical parameters of the double perovskite compounds Rb_2YAuBr_6 [panel a)], and Rb_2YAuCl_6 [panel b)] using GGA (red lines) and mBJ (blue lines) potentials: real part of the dielectric function $\varepsilon_1(\omega)$, imaginary part of the dielectric function $\varepsilon_2(\omega)$, refractive index $n(\omega)$ and extinction coefficient $K(\omega)$.

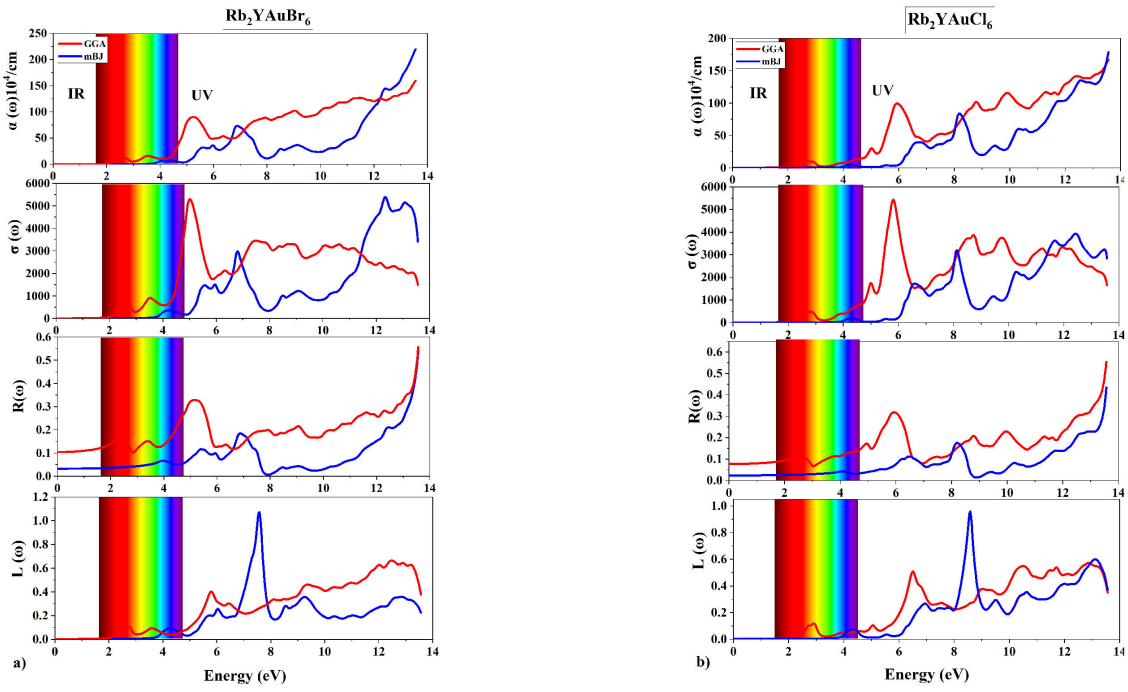

FIGURE 7. The calculated optical functions of the double perovskite compounds Rb_2YAuBr_6 [panel a)] and Rb_2YAuCl_6 [panel b)] using GGA (red lines) and mBJ (blue lines) potentials: absorption coefficient $\alpha(\omega)$, optical conductivity $\sigma(\omega)$, reflectivity $R(\omega)$ and energy loss function $L(\omega)$.

are similar. These optical constants suggest that both compounds possess the properties necessary for ultraviolet (UV) transparency and low reflectance. Further insights are provided by the absorption coefficient $\alpha(\omega)$, optical conductivity $\sigma(\omega)$, and energy loss function $L(\omega)$ [41]. All of which are depicted in Figs. 7a), 7b). The absorption spectra confirm that both materials exhibit sharp optical band edges in the near-UV region. The $\alpha(\omega)$ values exceed 150×10^4 cm^{-1}

in the far-UV region, which is comparable to that of known UV-absorbing semiconductors. The steep rise in $\alpha(\omega)$ reflects strong interband transitions and indicates the high purity of the simulated crystal structures. The optical conductivity $\sigma(\omega)$ increases significantly beyond the band edge, with pronounced peaks observed between 6 and 12 eV, particularly under mBJ. This suggests efficient carrier excitation. The energy loss function $L(\omega)$, which represents plasmonic behavior, reveals distinct peaks at approximately 7.8 and 8.2 eV for Rb_2YAuBr_6 and Rb_2YAuCl_6, respectively. These peaks are attributed to bulk plasmon resonances. The bromide compound's stronger, sharper peak suggests enhanced energy loss efficiency and potential applications in plasmonic and energy-harvesting devices. Overall, both materials demonstrate promising optical properties for use in ultraviolet photodetectors, solar-blind sensors, and optoelectronic devices. Furthermore, mBJ results provide a more accurate depiction of their spectral responses.

3.4. Elastic and mechanical properties

We evaluated the mechanical stability of the compounds by calculating their elastic constants using standard procedures [42, 43]. For cubic crystal systems, stability is determined by three independent elastic constants: C_{11}, C_{12} and C_{44}. A cubic crystal must satisfy the Born stability criteria to be mechanically stable:

$$C_{11} - C_{12} > 0, \quad C_{44} > 0, \tag{4}$$

$$C_{11} + C_{12} > 0, \quad 0 < B < C_{12}, \tag{5}$$

All of these are derived using standard relations [44].

$$B_V = \frac{C_{11} + 2C_{12}}{3}, \tag{6}$$

$$B_R = B_V, \tag{7}$$

$$B_0 = \frac{B_V + B_R}{2}, \tag{8}$$

$$G_V = \frac{1}{3}(3C_{44} + C_{11} - C_{12}), \tag{9}$$

$$G_R = \frac{5(C_{11} - C_{12})C_{44}}{4C_{44} + 3(C_{11} - C_{12})}, \tag{10}$$

$$G = \frac{G_V + G_R}{2}, \tag{11}$$

$$E = \frac{9BG}{3B + G}, \tag{12}$$

$$\nu = \frac{3B - 2G}{2(3B + G)}, \tag{13}$$

$$T_m = [553\,K + (5.911)C_{11}]GPa \pm 300\,K, \tag{14}$$

As shown in Table II, the bulk modulus, which quantifies resistance to uniform compression, is significantly higher for Rb_2YAuCl_6 (34.87 GPa) than for Rb_2YAuBr_6 (25.01 GPa). This suggests that the chloride-based compound has greater mechanical strength. This trend is consistent across the shear and Young's moduli, with Rb_2YAuCl_6 exhibiting superior stiffness overall. The B/G ratio provides further insight into ductility, with a critical threshold of 1.75 distinguishing between ductile and brittle materials [45, 46]. With a B/G ratio of 3.43, Rb_2YAuBr_6 clearly exhibits ductile behavior. In contrast, Rb_2YAuCl_6, with a ratio of 1.04, lies near the brittle limit. A similar pattern is observed in Poisson's ratio (ν): values above 0.26 typically indicate ductility and ionic bonding. The calculated Poisson's ratios are 0.367 for Rb_2YAuBr_6 and 0.137 for Rb_2YAuCl_6. These values suggest that Rb_2YAuBr_6 is more ductile and likely exhibits stronger ionic character, whereas Rb_2YAuCl_6 is more brittle, potentially due to greater contributions from covalent bonding. The estimated melting temperatures, 1200.42 K for Rb_2YAuCl_6 and 1057.85 K for Rb_2YAuBr_6, further support the superior thermal and mechanical resilience of the chloride compound. While both materials fulfill the criteria for mechanical stability, Rb_2YAuCl_6 is more thermally stable and mechanically robust, making it better suited to applications involving mechanical stress or high-temperature conditions.

3.5. Elastic anisotropy

To understand the directional mechanical behavior of the halide double perovskites Rb_2YAuBr_6 and Rb_2YAuCl_6, we analyzed their elastic anisotropy using three-dimensional (3D) representations of the following key mechanical moduli: Young's modulus (E), linear compressibility (β), shear modulus (G), and Poisson's ratio (ν). These results are shown in Fig. 8. These visualizations, obtained via the ELATE code [47], reveal deviations from spherical symmetry in all properties except β, indicating anisotropic behavior. This observation is quantitatively supported by the data summarized in Table III, which provides the extreme values and correspond-

TABLE II. Elastic constants (C_{ij}, B_0, G in GPa) and mechanical properties.

Compound	C_{11}	C_{12}	C_{44}	B_0	G	B/G	E (GPa)	ν	T_m (K)
Rb_2YAuBr_6	34.6	20.2	4.5	25.0	7.3	3.43	19.9	0.37	1058
Rb_2YAuCl_6	58.8	22.9	30.9	34.9	33.4	1.04	75.9	0.14	1200

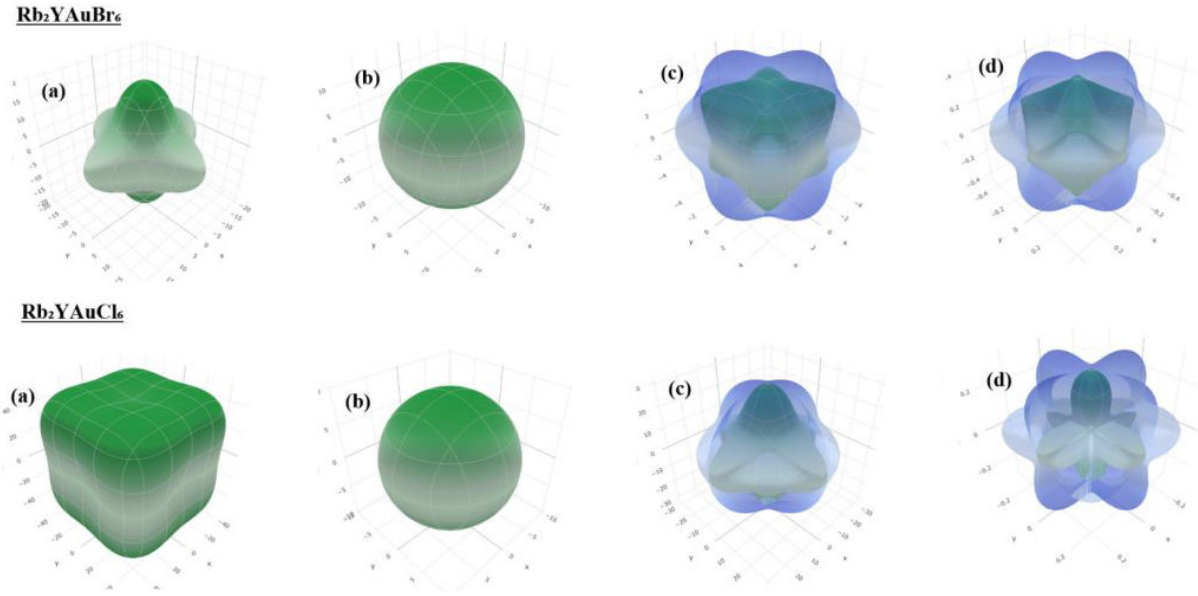

FIGURE 8. Calculated three-dimensional representations of the directional dependence of the elastic moduli for Rb_2YAuBr_6 and Rb_2YAuCl_6: a) Young's modulus, b) shear modulus, c) linear compressibility, and d) Poisson's ratio.

TABLE III. Anisotropic mechanical properties (Young's modulus E, Shear modulus G, Compressibility β, Poisson's ratio ν). Units in GPa except β (TPa^{-1}).

Property	Rb_2YAuBr_6	Rb_2YAuCl_6
Young's modulus *(E)*		
$E_{\min}$	12.684	45.917
$E_{\max}$	19.787	71.489
Anisotropy	1.560	1.557
Shear modulus *(G)*		
$G_{\min}$	4.4806	17.929
$G_{\max}$	7.2312	30.859
Anisotropy	1.614	1.721
Linear compressibility *(β)*		
$\beta_{\min}$	13.326	9.5593
$\beta_{\max}$	13.326	9.5593
Anisotropy	1.0000	1.0000
Poisson's ratio *(ν)*		
$\nu_{\min}$	0.2592	0.0167
$\nu_{\max}$	0.5550	0.3833
Anisotropy	2.1407	22.894

ing anisotropy factors for each property. For Rb_2YAuBr_6, the anisotropy is moderate, with values of 1.56 for Young's modulus and 1.614 for the shear modulus. The 3D plot of Poisson's ratio shows some directional distortion, consistent with an anisotropy factor of 2.14. In contrast, Rb_2YAuCl_6 exhibits more pronounced anisotropy, particularly in the shear modulus (1.721) and Poisson's ratio, which reaches an exceptionally high value of 22.89. This reflects significant variation in lateral deformation depending on the crystallographic direction. Notably, linear compressibility (β) is perfectly isotropic in both compounds, with an anisotropy factor of 1.000, as demonstrated by the nearly spherical shapes in the β plots. In conclusion, the numerical values in Table III and the visual evidence in Fig. 8 confirm that Rb_2YAuCl_6 exhibits stronger elastic anisotropy than Rb_2YAuBr_6, particularly in shear and deformation behavior. This anisotropy is a critical factor to consider when evaluating these materials for applications subject to complex stress fields [47-49].

3.6. Thermodynamic properties

Understanding the thermodynamic properties of materials is essential for evaluating their long-term effectiveness and stability in energy conversion processes under different environmental conditions. The Debye temperature ($\theta_{\rm D}$) can be used to estimate the strength of chemical bonds directly using the following expression [50]:

$$\theta_{\rm D} = f(\rho, M, v_m), \tag{15}$$

As demonstrated, $\theta_{\rm D}$ is related to material density (ρ), molar mass (M), and mean sound velocity (v_m) [50]. This relationship establishes a connection between $\theta_{\rm D}$ and these properties.

Figure 9 illustrates the temperature-dependent thermodynamic properties, including heat capacity (C_V), entropy (S), Debye temperature ($\theta_{\rm D}$), and thermal expansion coefficient (α) for Rb_2YAuX_6 (X = Br, Cl). These results, obtained using the quasi-harmonic Debye model over a wide temperature range (0–1800 K), reveal the effects of hydrostatic pressures ranging from 0 to 25 GPa. The heat capacity exhibits a sharp increase at low temperatures ($T < 300$ K), attributed to the progressive excitation of phonon modes. Beyond approximately 400 K, C_V tends to saturate near the classical Dulong–Petit limit of $3R$ per atom (approximately

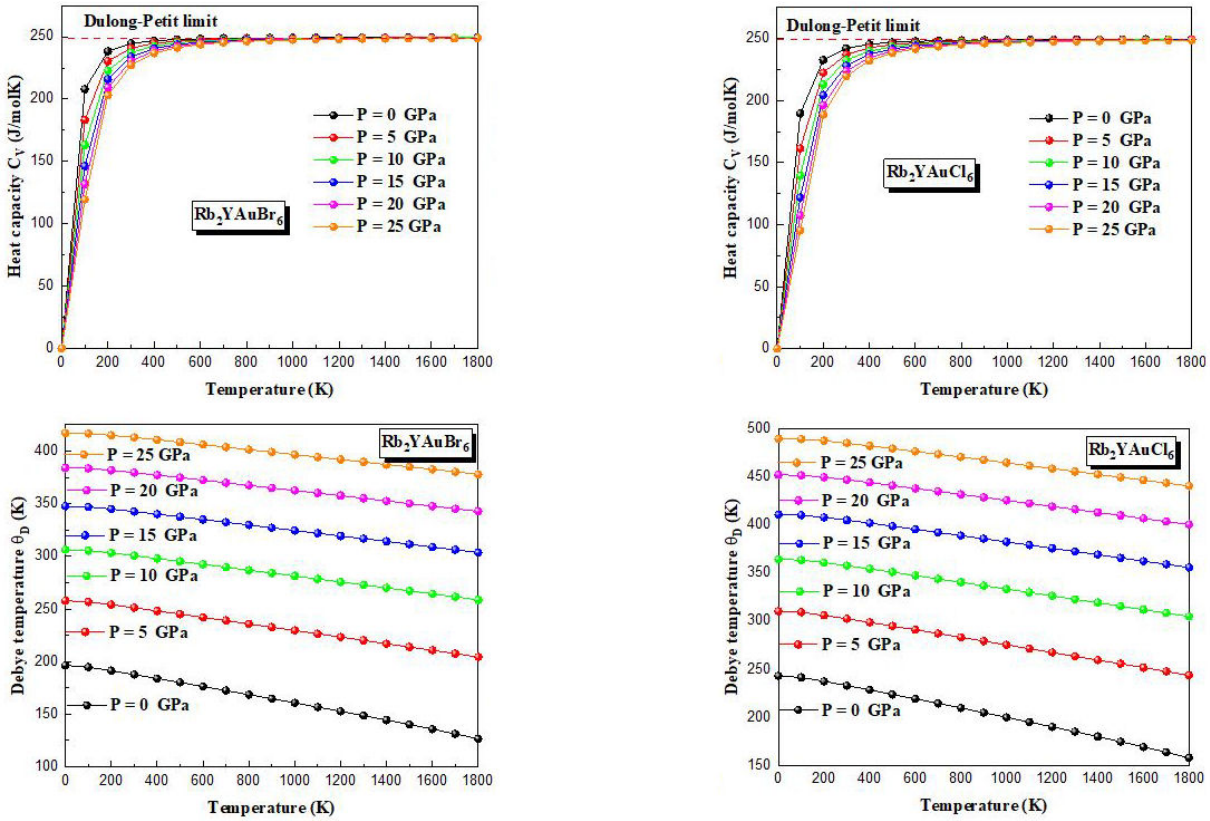

FIGURE 9. Variation against temperature in heat capacity and Debye temperature for Rb_2YAuX_6 (X = Br, Cl).

250 J/mol·K), consistent with the harmonic approximation at high temperatures. The influence of pressure is more noticeable at low temperatures, where increased pressure reduces the heat capacity, likely due to phonon stiffening caused by lattice compression. Of the two materials, Rb_2YAuCl_6 approaches saturation slightly faster than Rb_2YAuBr_6, reflecting differences in lattice dynamics and bond strengths related to the halide anion. The Debye temperature (θ_D), which reflects the average phonon frequency and thus the stiffness of the crystal lattice, shows an inverse correlation with temperature [51]. It decreases gradually with increasing temperature due to anharmonic effects and thermal expansion, which weaken interatomic bonds. However, θ_D systematically increases with applied pressure, consistent with lattice hardening and the suppression of low-frequency phonon modes. Rb_2YAuCl_6 exhibits consistently higher Debye temperatures than Rb_2YAuBr_6 at all pressures, indicating stronger bonding interactions and a more rigid framework in the chloride-based structure.

Figure 10 illustrates the relationship between entropy (S) and temperature. As is typical of crystalline solids, entropy increases monotonically with temperature as vibrational disorder intensifies. However, applying pressure significantly reduces entropy values as compressive stress restricts atomic vibrations and reduces configurational disorder. At equivalent temperatures and pressures, Rb_2YAuBr_6 exhibits higher entropy values than Rb_2YAuCl_6. This suggests that the bromide compound has a more disordered structure or a softer bonding environment. For instance, at 1000 K and 0 GPa, Rb_2YAuBr_6 has notably higher entropy than Rb_2YAuCl_6, which lends weight to this interpretation.

The thermal expansion coefficient α, shown in the final column, provides insight into the anharmonicity of lattice vibrations and the strength of interatomic bonding. Both compounds exhibit a sharp increase in α at low temperatures (up to $\sim$300 K), followed by either a plateau or a gradual increase at higher temperatures. This indicates saturation behavior, caused by the complete activation of phonon modes. The influence of pressure on α is significant; increased pressure leads to a substantial reduction in the thermal expansion coefficient [52, 53].

At room temperature (300 K), α values decrease systematically from ambient pressure to 25–30 GPa. For example, the α value of Rb_2YAuBr_6 is approximately 12.5×10^{-5} K^{-1} at 300 K and 0 GPa, decreasing to around 7×10^{-5} K^{-1} at 25 GPa. Rb_2YAuCl_6 exhibits lower α values under all conditions compared to its bromide counterpart, reflecting stronger interatomic forces and better thermal dimensional stability. These findings suggest that Rb_2YAuCl_6 is better suited to applications requiring structural rigidity and thermal stability under compressive stress. Conversely, Rb_2YAuBr_6, with its greater entropy and thermal expansivity, may be advantageous in systems requiring enhanced vibrational and thermal responsiveness.

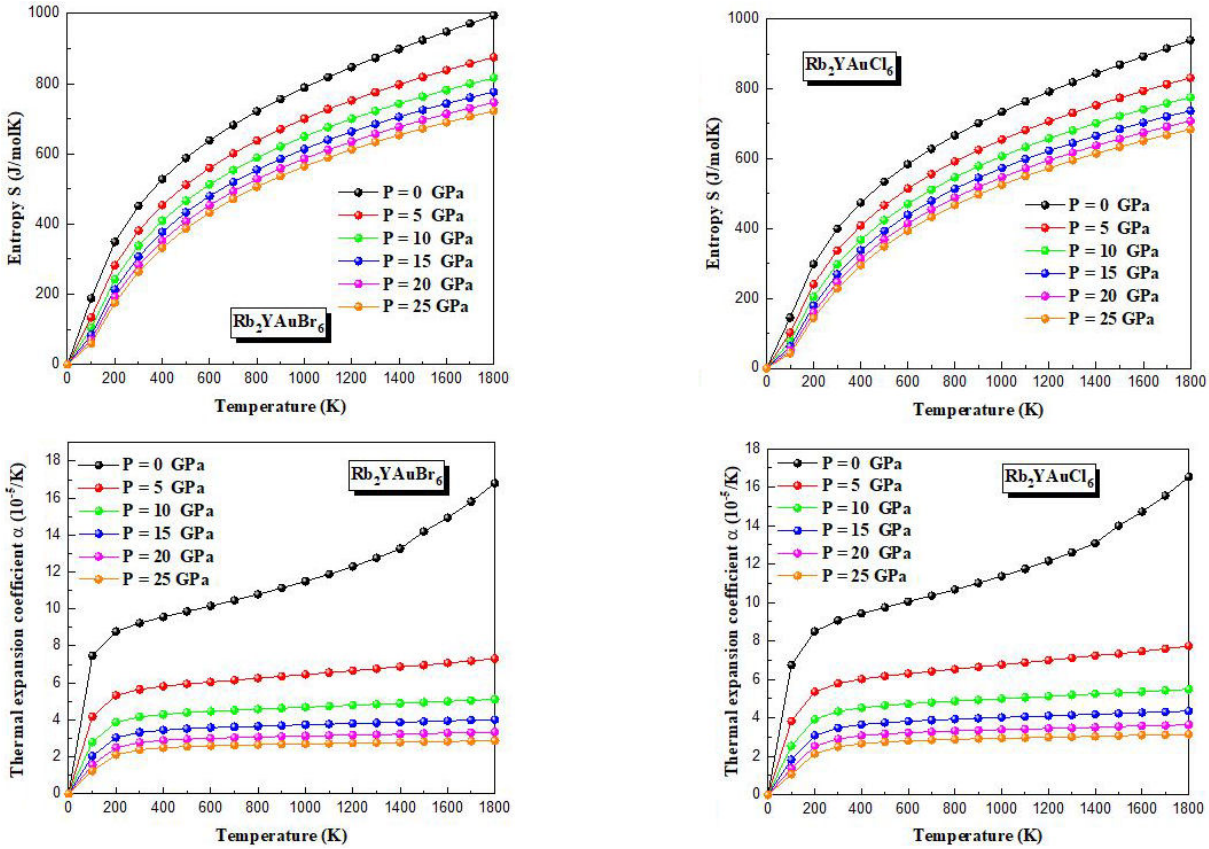

FIGURE 10. Variation against temperature in entropy and thermal expansion coefficient for Rb_2YAuX_6 (X = Br, Cl).

4. Conclusion

This study used density functional theory (DFT) to analyze the structural, thermodynamic, elastic and electro-optical properties of the halide double perovskite Rb_2YAuX_6 (X = Cl, Br). The results indicate that halide substitution has a significant impact on the mechanical behavior, thermal stability and optoelectronic performance of these materials. Calculations of elastic constants and formation energies confirm that both compounds crystallize in a mechanically stable cubic structure. While Rb_2YAuBr_6 and Rb_2YAuCl_6 both satisfy the criteria for mechanical stability, Rb_2YAuCl_6 exhibits superior ductility and thermal stability. This makes it a more suitable candidate for use in applications involving mechanical stress and elevated temperatures.

Thermodynamic evaluations further confirm their high-temperature stability, reinforcing their potential for industrial deployment. Furthermore, Rb_2YAuCl_6 exhibits stronger elastic anisotropy than Rb_2YAuBr_6 with regard to shear and deformation behavior. This is an important factor for devices operating under complex mechanical conditions. Band structure calculations show that both compounds are indirect band gap semiconductors. Within the GGA approximation, their band gaps range from 1.58 eV to 2.01 eV. However, the mBJ functional corrects these values to a higher range of 3.49–3.70 eV. Replacing Cl with Br reduces the band gap, indicating stronger optical absorption and a lower threshold for electronic excitation

While their absorption in the visible spectrum is limited under the GGA approximation, the mBJ-corrected results highlight the potential of these materials for optoelectronic applications, particularly in UV-light-driven photovoltaic devices. In conclusion, Rb_2YAuX_6 compounds demonstrate promising photoelectric and thermo-mechanical properties, establishing them as promising candidates for next-generation energy harvesting and optoelectronic technologies.

Acknowledgments

This work was supported by the Algerian University Research Project (PRFU) under grant number B00L02UN020120220004 and the General Directorate for Scientific Research and Technological Development (DGRSDT), Algeria `https://www.mesrs.dz/en/dgrsdt`.

Conflict of interest

The authors declare that they have no conflict of interest.

1. D. S. Ginley and C. Bright, Transparent conducting oxides, *MRS Bull.* **25** (2000) 15, https://doi.org/10.1557/mrs2000.227
2. T. Minami, Transparent conducting oxide semiconductors for transparent electrodes, *Semicond. Sci. Technol.* **20** (2005) S35, https://doi.org/10.1088/0268-1242/20/4/S03
3. M. Nolan and S. D. Elliott, The p-type conduction mechanism in $CuAlO_2$, *Phys. Chem. Chem. Phys.* **8** (2006) 5350, https://doi.org/10.1039/B609567J
4. S. D. Mo and W. Y. Ching, Electronic and optical properties of three phases of alumina, *Phys. Rev. B* **51** (1995) 13023, https://doi.org/10.1103/PhysRevB.51.13023
5. S. R. Pendharkar, et al., Spinel oxides in photovoltaics and photocatalysis, *J. Mater. Chem. A* **10** (2022) 10975, https://doi.org/10.1039/D2TA02138D
6. R. H. French, Electronic band structure of AlO with comparison to AlON and AlN, *J. Am. Ceram. Soc.* **73** (1990) 477, https://doi.org/10.1111/j.1151-2916.1990.tb06575.x
7. J. Robertson and S. J. Clark, Limits to doping in oxides, *Phys. Rev. B* **83** (2011) 075205, https://doi.org/10.1103/PhysRevB.83.075205
8. S. Kim, et al., Electronic structure and optical properties of spinel oxides: ZnAlO and ZnGaO, *J. Phys. Condens. Matter* **21** (2009) 195403, https://doi.org/10.1088/0953-8984/21/19/195403
9. N. Ueda, et al., Transparent p-type semiconducting CuAlO thin films prepared by pulsed laser deposition, *Appl. Phys. Lett.* **70** (1997) 3561, https://doi.org/10.1063/1.119435
10. C. H. Bhosale, et al., Preparation and characterization of CdO thin films by spray pyrolysis, *Mater. Chem. Phys.* **78** (2002) 122, https://doi.org/10.1016/S0254-0584(02)00352-5
11. J. E. F. Rodrigues, C. A. Escanhoela, Jr., B. Fragoso, G. Sombrio, M. M. Ferrer, C. Álvarez-Galván, and J. A. Alonso, Experimental and Theoretical Investigations on the Structural, Electronic, and Vibrational Properties of $Cs_2AgSbCl_6$ Double Perovskite, *Ind. Eng. Chem. Res.* **60** (2021) 18918, https://doi.org/10.1021/acs.iecr.1c02188
12. G. Volonakis, M. R. Filip, A. A. Haghighirad, N. Sakai, B. Wenger, H. J. Snaith, and F. Giustino, $Cs_2InAgCl_6$: A New Lead-Free Halide Double Perovskite with Direct Band Gap, *J. Phys. Chem. Lett.* **8** (2017) 772, https://doi.org/10.1021/acs.jpclett.6b02682
13. H. -J. Feng, W. Deng, K. Yang, J. Huang, and X. C. Zeng, Double Perovskite Cs_2BBiX_6 (B = Ag, Cu; X = Br, Cl)/TiO_2 Heterojunction: An Efficient Pb-Free Perovskite Interface for Charge Extraction, *J. Phys. Chem. C* **121** (2017) 4471, https://doi.org/10.1021/acs.jpcc.7b00138
14. E. McClure, M. R. Ball, W. Windl, and P. M. Woodward, Cs_2AgBiX_6 (X = Br, Cl): New Visible Light Absorbing, Lead-Free Halide Perovskite Semiconductors, *Chem. Mater.* **28** (2016) 1348, https://doi.org/10.1021/acs.chemmater.5b04231
15. B. Wang, N. Li, L. Yang, C. Dall'Agnese, A. K. Jena, S. I. Sasaki, and X. F. Wang, Chlorophyll derivative-sensitized TiO_2 electron transport layer for record efficiency of $Cs_2AgBiBr_6$ double perovskite solar cells, *J. Am. Chem. Soc.* **143** (2021) 2207, https://doi.org/10.1021/jacs.0c12786
16. G. García-Espejo, D. Rodríguez-Padrón, R. Luque, L. Camacho, G. de Miguel, Mechanochemical synthesis of $Cs_2AgBiBr_6$, $(CH_3NH_3)_2TlBiBr_6$ and $Cs_2AgSbBr_6$, *Nanoscale* **11** (2019) 16650. https://doi.org/10.1039/C9NR06092H
17. X. Diao, Y. Tang, Q. Gu, Y. Shi, and P. Zhu, Structural, stability, electronic and optoelectronic properties of Y_2AgBiX_6 (Y = K, Na, Li; X = I, Br, Cl): a first-principles study, *Solar Energy* **262** (2023) 111914, https://doi.org/10.1016/j.solener.2023.111914
18. Z. Xiao, K. Z. Du, W. Meng, J. Wang, D. B. Mitzi, and Y. Yan, Intrinsic instability of $Cs_2In(I)M(III)X_6$ (M = Bi, Sb; X = halogen), *J. Am. Chem. Soc.* **139** (2017) 6054, https://doi.org/10.1021/jacs.7b02227
19. M. Saeed, I. U. Haq, A. S. Saleemi, S. U. Rehman, B. U. Haq, A. R. Chaudhry, and I. Khan, First-principles prediction of the ground-state structure of Cs_2AgCrX_6 (X = Cl, Br, I), *J. Phys. Chem. Solids* **160** (2022) 110302, https://doi.org/10.1016/j.jpcs.2021.110302
20. A. Ayyaz, G. Murtaza, M. Shafiq, M. Q. Shah, N. Sfina, and S. Ali, Structural, thermodynamic, elastic, electro-optic and thermoelectric properties of Rb_2XInBr_6 (X = Na, K), *Solar Energy* **265** (2023) 112131, https://doi.org/10.1016/j.solener.2023.112131
21. A. Ayyaz, G. Murtaza, A. Usman, M. Umer, M. Q. Shah, and H. S. Ali, First principles insight on mechanical stability, optical and thermoelectric response of lead-free $Rb_2ScCuBr_6$ and $Cs_2ScCuBr_6$, *Mater. Sci. Semicond. Process.* **169** (2024) 107910, https://doi.org/10.1016/j.mssp.2023.107910
22. M. W. Iqbal, M. Manzoor, S. Gouadria, M. Asghar, M. Zainab, N. N. Ahamd, and T. Zahid, DFT insights on opto-electronic and thermoelectric properties of K_2AgSbX_6 (X = Cl, Br), *Mater. Sci. Eng. B* **290** (2023) 116338, https://doi.org/10.1016/j.mseb.2023.116338
23. S. Grimme, Semiempirical GGA-type density functional with long-range dispersion correction, *J. Comput. Chem.* **27** (2006) 1787, https://doi.org/10.1002/jcc.20495
24. J. P. Perdew, K. Burke, and M. Ernzerhof, Generalized gradient approximation made simple, *Phys. Rev. Lett.* **77** (1996) 3865, https://doi.org/10.1103/PhysRevLett.77.3865
25. J. P. Perdew, A. Ruzsinszky, G. I. Csonka, O. A. Vydrov, and G. E. Scuseria, Restoring the density-gradient expansion for exchange in solids, *Phys. Rev. Lett.* **100** (2008) 136406; Erratum **102** (2009) 039902, https://doi.org/10.1103/PhysRevLett.100.136406
26. F. Tran and P. Blaha, Accurate band gaps using semilocal exchange-correlation potential, *Phys. Rev. Lett.* **102** (2009) 226401, https://doi.org/10.1103/PhysRevLett.102.226401

27. H. J. Monkhorst and J. D. Pack, Special points for Brillouin-zone integrations, *Phys. Rev. B* **13** (1976) 5188, https://doi.org/10.1103/PhysRevB.13.5188

28. M. Jamal, S. J. Asadabadi, I. Ahmad, and H. A. Rahnamaye Aliabad, Elastic constants of cubic crystals, *Comput. Mater. Sci.* **95** (2014) 592, https://doi.org/10.1016/j.commatsci.2014.08.027

29. V. Lucarini, J. J. Saarinen, K. E. Peiponen, and E. M. Vartiainen, *Kramers-Kronig Relations in Optical Materials Research* (Springer, 2005), Vol. 110, https://doi.org/10.1007/b138245

30. A. Otero-De-La-Roza, D. Abbasi-Pérez, and V. Luaña, Gibbs2: quasiharmonic thermodynamics code, *Comput. Phys. Commun.* **182** (2011) 2232, https://doi.org/10.1016/j.cpc.2011.05.009

31. V. M. Goldschmidt, Die gesetze der krystallochemie, *Naturwissenschaften* **14** (1926) 477, https://doi.org/10.1007/BF01507527

32. R. D. Shannon, Revised effective ionic radii, *Acta Cryst.* **32** (1976) 751, https://doi.org/10.1107/S0567739476001551

33. C. Li, X. Lu, W. Ding, L. Feng, Y. Gao, and Z. Guo, Formability of ABX_3 halide perovskites, *Acta Cryst. B* **64** (2008) 702, https://doi.org/10.1107/S0108768108032734

34. K. Ouchetto, F. Archaimbault, A. Pineau, and J. Choisnet, Chemical and structural characterization of Ba_2CePtO_6, *J. Mater. Sci. Lett.* **10** (1991) 1277, https://doi.org/10.1007/BF00720945

35. F. D. Murnaghan, The compressibility of media under extreme pressures, *Proc. Natl. Acad. Sci. USA* **30** (1944) 244, https://doi.org/10.1073/pnas.30.9.244

36. N. Reyren, et al., Superconducting interfaces between insulating oxides, *Science* **317** (2007) 1196, https://doi.org/10.1126/science.1146006

37. T. Ou, Q. Zhuang, H. Yan, S. Feng, P. Li, and X. Ma, Lead-free Rb_2InSbX_6 double perovskites, *Chem. Phys.* **573** (2023) 112015, https://doi.org/10.1016/j.chemphys.2023.112015

38. A. Boutramine, et al., Optoelectronic and thermoelectric properties of K_2NaSbZ_6 (Z = Br, I), *Opt. Quant. Electron.* **56** (2024) 417, https://doi.org/10.1007/s11082-024-06344-4

39. M. Hilal, B. Rashid, S. H. Khan, and A. Khan, Electro-optical properties of InSb with spin-orbit effects, *Mater. Chem. Phys.* **184** (2016) 41, https://doi.org/10.1016/j.matchemphys.2016.09.009

40. Q. Mahmood, et al., Electronic and thermoelectric properties of $K_2Pd(Cl/Br)_6$, *Phys. Scr.* **97** (2022) 035803, https://iopscience.iop.org/article/10.1088/1402-4896/ac4ed3

41. G. Murtaza, et al., Band gap tailoring in $Sr_{1-x}Ba_xSnO_3$, *Chem. Phys.* **551** (2021) 111322, https://doi.org/10.1016/j.chemphys.2021.111322

42. M. Gajdoš, K. Hummer, G. Kresse, J. Furthmüller, and F. Bechstedt, Linear optical properties in PAW method, *Phys. Rev. B* **73** (2006) 045112, https://doi.org/10.1103/PhysRevB.73.045112

43. M. Born and K. Huang, *Dynamical Theory of Crystal Lattices* (Clarendon Press, Oxford, 1954), pp. 837–838.

44. S. I. Ranganathan and M. Ostoja-Starzewski, Universal elastic anisotropy index, *Phys. Rev. Lett.* **101** (2008) 055504, https://doi.org/10.1103/PhysRevLett.101.055504

45. R. Hill, Elastic behaviour of crystalline aggregates, *Proc. Phys. Soc. A* **65** (1952) 349, https://doi.org/10.1088/0370-1298/65/5/307

46. S. F. Pugh, Relations between elastic moduli and plastic properties, *Philos. Mag.* **45** (1954) 823, https://doi.org/10.1080/14786440808520496

47. R. Gaillac, P. Pullumbi, and F. X. Coudert, ELATE: elastic tensor visualization tool, *J. Phys.: Condens. Matter* **28** (2016) 275201, https://doi.org/10.1088/0953-8984/28/27/275201

48. C. M. Zener and S. Siegel, Elasticity and anelasticity of metals, *J. Phys. Chem.* **53** (1949) 1468, https://doi.org/10.1021/j150474a017

49. M. E. Fine, L. D. Brown, and H. L. Marcus, Elastic constants versus melting temperature in metals, *Scripta Metall.* **18** (1984) 951, https://doi.org/10.1016/0036-9748(84)90267-9

50. C. Jasiukiewicz and V. Karpus, Debye temperature of cubic crystals, *Solid State Commun.* **128** (2003) 167, https://doi.org/10.1016/j.ssc.2003.08.008

51. D. G. Cahill, S. K. Watson, and R. O. Pohl, Lower limit to thermal conductivity of disordered crystals, *Phys. Rev. B* **46** (1992) 6131, https://doi.org/10.1103/PhysRevB.46.6131

52. A. Otero-de-la-Roza and V. Luaña, Robust treatment of static data in Gibbs2, *Comput. Phys. Commun.* **182** (2011) 1708, https://doi.org/10.1016/j.cpc.2011.04.016

53. M. A. Blanco, E. Francisco, and V. Luaña, GIBBS: quasi-harmonic Debye model, *Comput. Phys. Commun.* **158** (2004) 57, https://doi.org/10.1016/j.comphy.2003.12.001